Interlocking-Governed Ultra-Strong and Highly Conductive MXene Fibers Through Fluidics-Assisted Thermal Drawing

Tianzhu Zhou[1], Can Cao[4], Shixing Yuan[1], Zhe Wang[1], Qi Zhu[6], Hao Zhang[3], Jia Yan[2], Fan Liu[1], Ting Xiong[1], Qunfeng Cheng[2,5], and Lei Wei[1,7*]*

[1]School of Electrical and Electronic Engineering, Nanyang Technological University, Singapore 639798, Singapore

[2]School of Chemistry, Key Laboratory of Bio-inspired Smart Interfacial Science and Technology of Ministry of Education, Beihang University, Beijing 100191, China

[3]Research Institute of Chemical Defense, Beijing 100191, China

[4]School of Materials Science and Engineering, Nanyang Technological University, Singapore 639798, Singapore

[5]Suzhou Institute for Advanced Research, University of Science and Technology of China, Suzhou 215123, China

[6]School of Mechanical and Aerospace Engineering, College of Engineering, Nanyang Technological University, Singapore 639798, Singapore

[7]The Institute for Digital Molecular Analytics and Science (IDMxS), Nanyang Technological University, 636921, Singapore

*E-mail: wei.lei@ntu.edu.sg; cheng@buaa.edu.cn

Keywords: MXene nanosheets, fibers, mechanical property and electrical conductivity, electromagnetic interference shielding

Abstract

High-performance MXene fibers are always of significant interest for flexible textile-based devices. However, achieving high mechanical property and electrical conductivity remains challenging due to the uncontrolled loose microstructures of MXene nanosheets. Herein, we demonstrate high-performance MXene fibers directly obtained through fluidics-assisted thermal drawing. Tablet interlocks are formed at the interface layer between the outer cyclic olefin copolymer and inner MXene nanosheets due to the thermal drawing induced stresses, resulting in thousands of meters long macroscopic compact MXene fibers with ultra-high tensile strength, toughness, and outstanding electrical conductivity. Furthermore, large-scale

woven textiles constructed by these fibers offer exceptional electromagnetic interference shielding performance with excellent durability and stability. Such an effective and sustainable approach can be applied to produce functional fibers for applications in both daily life and aerospace.

1. Introduction

Macroscopic MXene fibers can be manufactured through fluidics-assisted assembling processes from individual MXene nanosheets in solutions because of their surface-terminated moieties (T_x) including -OH, -O, and -F,[1] potentially engaged in developing flexible textile-based devices with high mechanical,[2] electrical,[3] and electromagnetic properties.[4] Due to the liquid-crystal behavior of the MXene solution, a macroscopic fiber with an ordered structure could be directly formed under the shear flow with the pre-aligned MXene nanosheets.[5,6] However, achieving precise control of the microstructures, including high alignment and low porosity between MXene nanosheets, is critical to obtain high mechanical and electrical properties for the assembled MXene fibers. Presently, some strategies have been demonstrated to fabricate macroscopic MXene fibers from MXene ($Ti_3C_2T_x$) nanosheets, for instance, wet spinning,[7] electrospinning,[8] thermal drawing,[9] coating,[10] and scrolling methods[11]. Although the macroscopic MXene fibers with desired mechanical properties and electrical conductivity have been successfully fabricated via the interaction with crosslinkers such as nanosheets,[12,13] ions,[5,14] and polymers[15-17]. Yet, it is challenging to maintain the intrinsic mechanical properties and electrical conductivity of MXene nanosheets for the macroscopic form factors due to their inherently loose layers of the microstructures. Therefore, the resulting loose structures, caused by the microstructure defects (such as voids and wrinkles) and poor interlayer interactions between MXene nanosheets, indeed limit the comprehensive promotion of mechanical and electrical properties of MXene fibers.

Additionally, functional textiles with macroscopic fibers that offer high mechanical and electrical performance are necessary to cover large areas of the human body or to meet the needs of precise instruments.[18] However, under extreme conditions and when in contact with human skin,[19] functional textiles experienced physical impact in the form of movements and deformation,[20,21] and were sensitive and fragile to washing and drying, which commonly resulted in the performance degradation of these fibers and prevented their long-term usage. An effective route to solve these problems is to fabricate macroscopic fibers with a layer of protection on their outer surface.[22] However, although the toughness and tensile strength of

macroscopic MXene fibers prepared with the protective layer were promoted, more microstructure defects such as wrinkles and voids, the residual water molecule, and crosslinkers remained in the interlayers of MXene nanosheets, resulting in poor electrical conductivity.[23] Recently, ultra-compact MXene fibers were demonstrated via a continuous and controllable manner involving wet spinning and thermal drawing.[24] However, it is hard to realize the full utility of the electrical conductivity of MXene nanosheets due to the introduction of crosslinkers as the binder to enhance the mechanical properties, and additional processing steps are still needed.

Herein, we demonstrate high-performance MXene fibers fabricated by a continuously one-step fluidics-assisted thermal drawing, as schematically exhibited in **Figure 1a**. Due to the spinnability of MXene/propylene carbonate (PC) slurry and thermal drawing induced stresses, the random MXene nanosheets are guided to form highly aligned MXene fibers by in-situ generating a cyclic olefin copolymer (COC) protective layer with highly oriented chains. More importantly, the tablet interlocks between the outer COC layer and inner MXene nanosheets are generated at the interface layer because of the thermal drawing stresses, obtaining ultra-long MXene fibers with high orientation and low porosity to significantly enhance both the mechanical and electrical properties. Next, large-scale functional textiles are woven by the resultant ultra-strong macroscopic MXene fibers for effective electromagnetic interference (EMI) shielding in high-performance applications.

2. Results

2.1. Characterization of MXene/PC slurry

Two types of MXene nanosheets ($Ti_3C_2T_x$ for CMXene and Ti_3CNT_x for NMXene) were fabricated through etching and shaking processes from preliminary materials of MAX (Ti_3AlC_2 and Ti_3AlCN) (Figure S1). After exfoliation, the CMXene and NMXene nanosheets show a lateral size of ~10.6 μm and ~8.1 μm with a thickness of ~1.8 nm and ~2.0 nm, respectively, according to the scanning electron microscope (SEM) and atomic force microscopy (AFM) images (Figure S2 and S3), with highly hexagonal structures without crystallinity defects (Figure S4).[25] Moreover, the disappeared characteristic peaks at 104 and 105 of X-ray diffraction (XRD) patterns for MXene nanosheets confirm the successful preparation of MXene nanosheets by completely etching the Al layer of the MAX phase (Figure S5).[26]

Because of the high dispersion stability of MXene nanosheets in dimethyl formamide (DMF) and PC solvent with high surface tension,[27,28] a slurry of MXene/PC with a high concentration of MXene was prepared through solvent exchange and centrifuging concentration processes (Figure S6). The slurry containing MXene concentration of 120-160 mg mL^{-1} shows the typical birefringence, suggesting the formation of a liquid-crystalline phase due to the orientation of MXene nanosheets without aggregation (Figure S7).[5] Similar to the conventional fluid systems consisting of rigid polymer chains,[29] the viscosity of the fresh slurry decreases with the increase of the shear rate, even at different heating temperatures from 25 ºC to 200 ºC (**Figure 1b** and Figure S8a). Moreover, the in-situ viscosity of MXene/PC at the concentration of 160 mg mL^{-1} shows a constant stage at the range of 25 ºC to 160 ºC, and then a slight decrease from 160 ºC to 200 ºC due to the weakened interactions between MXene nanosheets and PC solvent when heated (**Figure 1c**). Furthermore, the viscosity significantly increases because of the volatilization of PC solvent when heated up to 220 ºC, indicating good stability of the slurry system for spinnability. Furthermore, with an increasing shear rate, the shear stresses of slurry with the concentration of 160 mg mL^{-1} and COC polymer obviously decrease at the initial stage and then show a gradual increment (Figure S8b), indicating that the random MXene nanosheets and COC chains turn into more aligned due to the shear-induced deformation when drawing. In addition, the in-situ shear stress of the slurry presents a gradual decline at the stage of 160 ºC to 200 ºC and then significantly increases from 200 ºC to 220 ºC, suggesting an increased ordered state with high stability of MXene nanosheets when in-situ removing the PC solvent even at heating (Figure S8c). To quantify the spinnability of 2D liquid-crystalline colloidal dispersions, the storage modulus (G') to loss modulus (G'') ratio can be evaluated within the 1.80 to 6.36 range.[30,31] For example, the reported works have proven that the graphene oxide and MXene spinning dispersion at a high concentration can enable the fiber fabrication through wet spinning based on such a quantified factor. Here, the ratio of G'/G'' for the MXene/PC slurry with a high concentration can also be used as the indicator for the spinnability for thermal drawing when heated. As presented in **Figure 1d** and Figure S8d, for the slurry with the concentration of 160 mg mL^{-1}, when the slurry is heated at temperatures from 25 ºC to 220 ºC, the ratio of G'/G'' is in the range of 3.34 to 1.91, indicating the spinnability to form MXene fibers by thermal drawing. Also, the slurry with concentrations ranging from 120 mg mL^{-1} to 160 mg mL^{-1} still exhibits a G'/G'' of 4.04 to 1.82 during heating, suggesting its good stability and spinnability through thermal drawing. Meanwhile, COC polymer, as the outer protective layer, has higher storage modulus (G') and loss

modulus (G'') than MXene/PC slurry to confine the inner slurry without fracture in the thermal drawing procedure.

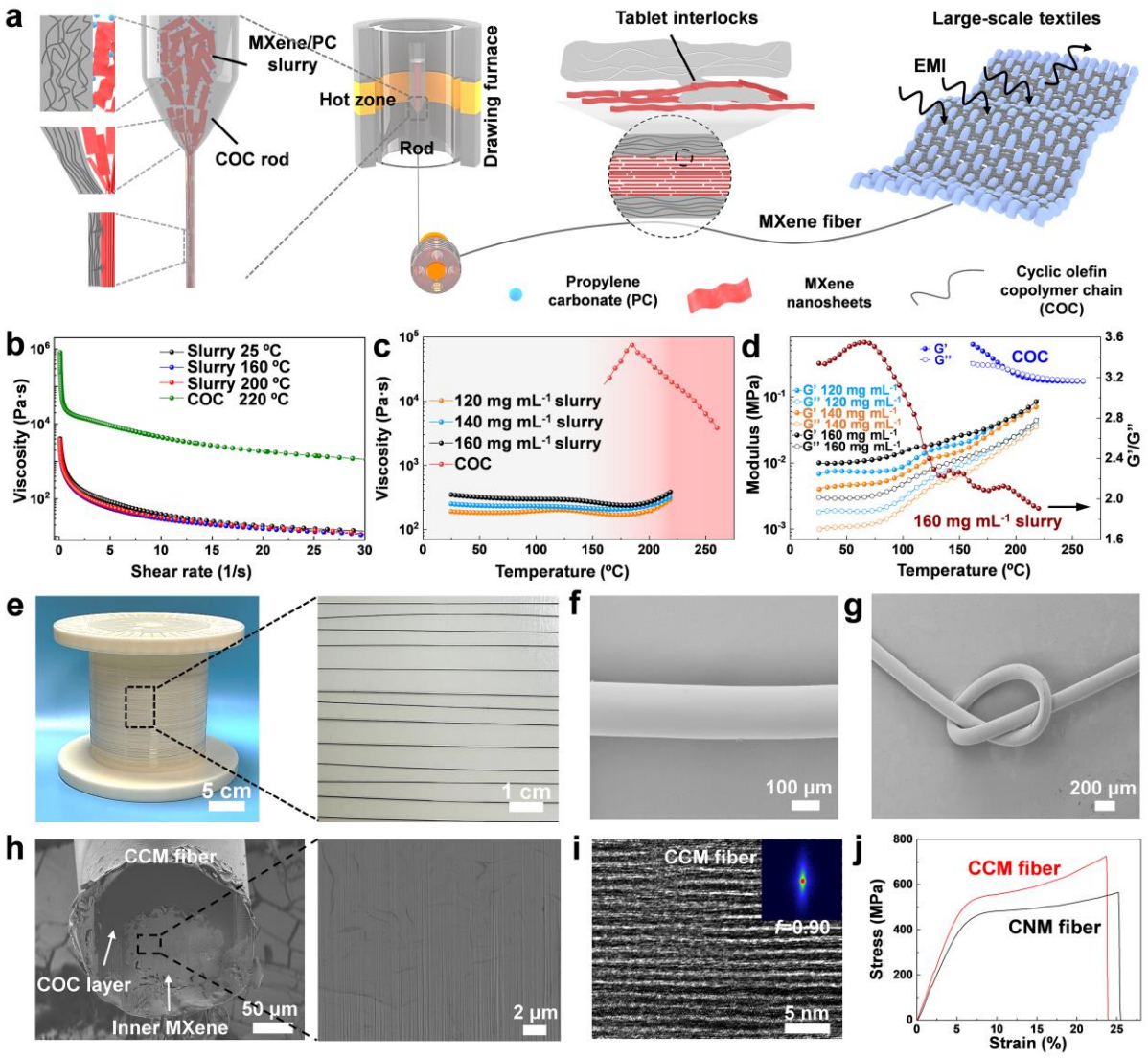

Figure 1. A process flow to fabricate strong macroscopic MXene fibers. a, Schematic diagram of fabrication of MXene fiber with tablet interlocks between outer COC layer and inner MXene fibers at the interface layer directly through fluidics-assisted thermal drawing, and the preparation of woven textiles based on strong MXene fibers. **b**, Viscosity vs. shear rate for MXene/PC slurry and COC. Viscosity (**c**), and storage modulus (G') and loss modulus (G'') (**d**) for MXene/PC slurry and COC at heating temperatures of 25 ºC to 260 ºC. **e**, Photography of larger-scale preparation of macroscopic MXene fibers. SEM images of the flattened (**f**) and twisted (**g**) MXene fibers. FIB-SEM cross-section (**h**) and HR-TEM image (**i**) of CCM fibers through thermal drawing. **j**, Stress-strain curves of CCM and CNM fibers through fluidics-assisted thermal drawing.

2.2. Fabrication of MXene fibers with COC protective layer

Based on the spinnability of the MXene/PC slurry in the heating process, large-scale macroscopic MXene fibers with good flexibility can be continuously fabricated from the slurry by gradually in-situ removing the PC solvent through fluidics-assisted thermal drawing (**Figure 1e-g** and Movie S1). With the assistance of thermal drawing induced stresses, macroscopic MXene fibers were achieved with the high alignment of the COC protective layer (CCM for COC-CMXene) and a diameter of ~210 μm, including an MXene fiber core with an inner diameter of ~110 μm, according to the focused ion beam-scanning electron microscopy (FIB-SEM) images in **Figure 1h**. The obtained MXene fiber core showed highly compact and aligned MXene nanosheet layers, as indicated in the high-resolution transmission electron microscopy (HR-TEM) image, with an orientation order (*f*) of 0.90 and a high tensile strength of 707.73 ± 18.33 MPa for CCM fiber and 566.55 ± 1.21 MPa for CNM (COC-NMXene) fiber thanks to the tablet interlocks at the interface layer between the COC layer and MXene nanosheets, as shown in **Figure 1i** and **1j**.

The solvent in the MXene/PC slurry can be slowly removed through volatilization when heating up to 220 ºC, according to the result of thermogravimetric analysis (TGA) (Figure S9). As indicated by the Fourier transform infrared spectroscopy (FTIR) spectra in Figure S10 and S11, there is no peak at ~1791.5 cm^{-1} for PC solvent in CCM fibers, inner CMXene fiber of CCM (ICMXene), CNM fiber, and inner NMXene fibers of CNM (INMXene), suggesting the successful removal of PC solvent through the thermal drawing. Moreover, CCM and CNM fibers with the characteristic peak at ~2944.0 cm^{-1}, ~2867.0 cm^{-1}, and ~1455.0 cm^{-1} for COC polymer prove the formation of a COC protective layer coating the inner MXene fibers. X-ray photoelectron spectroscopy (XPS) spectra confirm the successful preparation of MXene nanosheets, as no Al element is detected in fresh MXene nanosheets, ICMXene fiber, and INMXene fiber, compared with the spectra of MAX materials (Figure S12). Furthermore, there is no increasing atomic percentage for the O element of the inner MXene cores in CCM and CNM fibers, indicating the complete removal of PC solvent through the thermal drawing (Table S1). In addition, the low atomic percentages for Ti-O in Ti 2p spectra and C-Ti-OX/C-Ti-OH in O 1s spectra, are retained for the CCM and CNM fibers (Figure S13, S14, and Table S2-4), demonstrating hydrogen bonds between MXene nanosheets with -OH/F moieties. Both the atomic percentages for total Ti-O in Ti 2p spectra and C-Ti-OX/C-Ti-OH in O 1s spectra for the obtained inner CMXene fibers decrease to 18.60% and 31.77%, compared with that of fresh CMXene nanosheets including CNM fibers.

This indicates the removal of partial hydroxyl surface terminations and intercalated water of MXene nanosheets by the heat during thermal drawing.

2.3. Orientation and porosity of MXene fibers through thermal drawing

To study the morphology changes of MXene fibers during thermal drawing, in-situ XRD patterns were collected at different heating temperatures. When CMXene fibers were in the hot zone with a temperature up to 250 ºC, the pattern at 002 exhibited a high q shift with the decreasing d-spacing to 10.65 Å for MXene nanosheets under the increasing temperature (**Figure 2a** and Figure S15). The porosity of CMXene fibers sharply increased up to 15.3% with the heating temperature of 220 ºC, suggesting wrinkles and voids between MXene nanosheets were generated when heated. Similarly, NMXene fibers showed a decline of d-spacing and an increase of porosity when heated, as shown in Figure S16. Then, the increasing intensity of in-situ small-angle X-ray scattering (SAXS) patterns for these MXene fibers further confirmed the generation of voids at higher annealing temperatures (Figure S17).[32,33] The generation of voids between MXene nanosheets are mainly due to the slow removal of the partial hydroxyl surface terminations and intercalated water of MXene nanosheets when elevated temperatures were applied to fibers.[34]

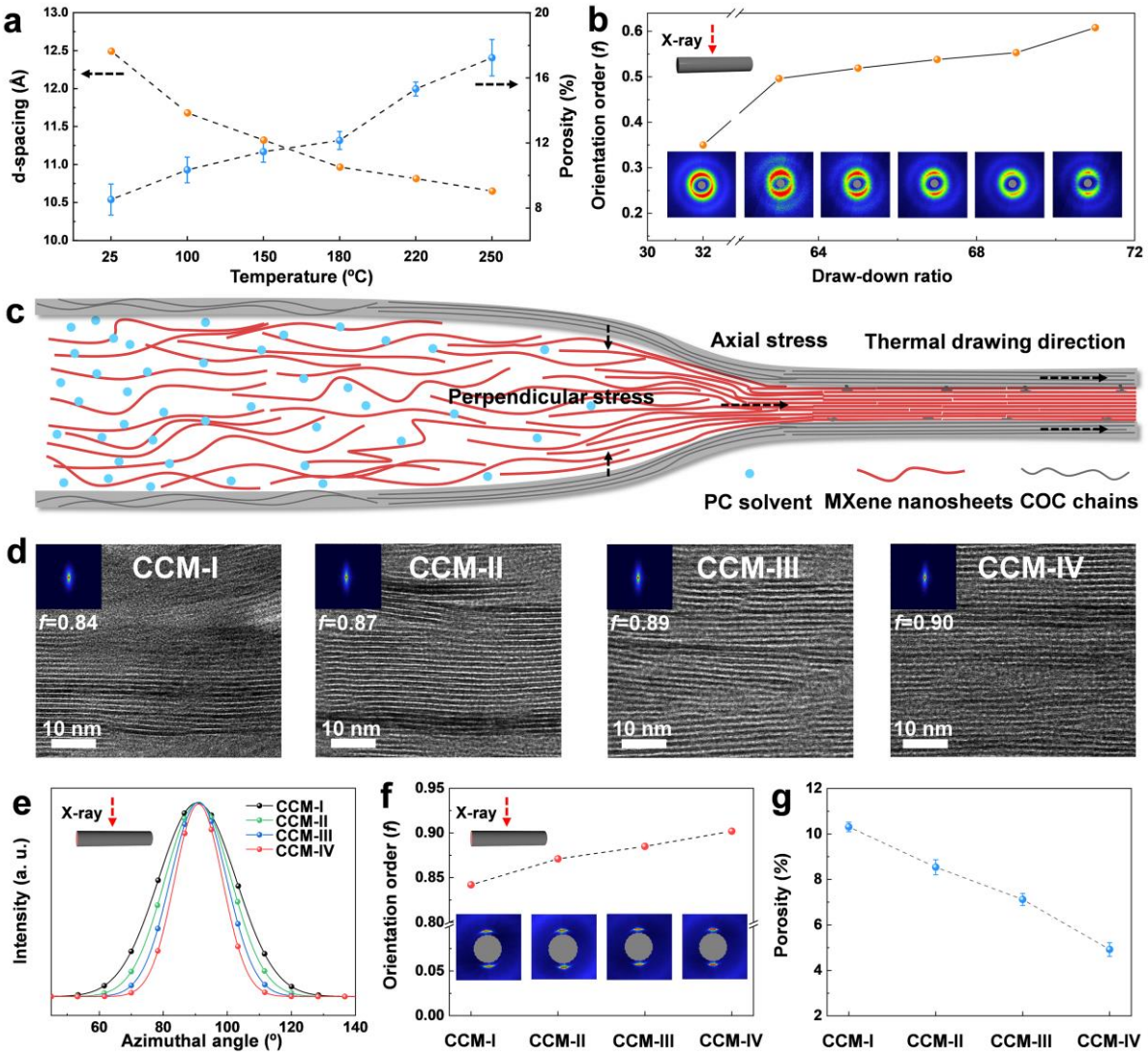

Figure 2. Orientation and porosity of MXene fibers through fluidics-assisted thermal drawing. **a**, d-spacing and porosity of pure fiber when heated. **b**, Orientation order (*f*) of COC fibers at different draw-down ratios shown by WAXS patterns (inset). **c**, Schematic diagram of mechanism to fabricate MXene fibers from MXene/PC slurry using axial and perpendicular stress during thermal drawing. **d**, HR-TEM images of CCM fibers with SAXS patterns (inset) at various draw-down ratios. **e**, Plots of azimuthal angle for CCM fibers fabricated via various draw-down ratios. Orientation order (**f**) based on the WAXS patterns (inset) and porosity (**g**) of CCM fibers.

After passing through the hot zone in the thermal drawing process, MXene nanosheets tend to achieve high orientation with low porosity, thanks to the thermal drawing induced stresses, such as axial and perpendicular stress. At the same time, the alignment of pure COC chains of the rod polymer is also significantly promoted, observed via the wide-angle X-ray scattering

(WAXS) patterns. When the draw-down ratio (*D*) (see Methods) was increased from 32 to 71, the orientation order (*f*) increased from 0.35 to 0.61 (**Figure 2b** and Figure S18), indicating the COC chains tended to align when thermal drawing stresses were applied to the COC layer. Therefore, the macroscopic MXene fibers were directly fabricated with a COC protective layer generated in-situ by thermal drawing, as presented in **Figure 2c**. More interestingly, due to the stresses, tablet interlocks were formed at the interface layers between outer COC layer and inner MXene nanosheets.

Through systematically optimizing the concentration of slurry within the 120-160 mg mL^{-1} range, fibers formed from the MXene/PC slurry by using the concentration of 160 mg mL^{-1} offer high mechanical and conductive properties because of the high orientation and low porosity (Figure S19-24 and Table S5-7).[35] Based on the optimum concentration of 160 mg mL^{-1}, the macroscopic CCM fibers were fabricated by the thermal drawing with various draw-down ratios of 65, 67, 69, and 71, denoted as CCM-I, CCM-II, CCM-III, and CCM-IV. Benefiting from the larger thermal drawing induced stresses, the alignment of MXene nanosheets is further improved according to the HR-TEM and SAXS patterns of the inner MXene fibers, as shown in **Figure 2d** and Figure S25. For example, with the increasing draw-down ratio, *f* increases from 0.84 to 0.90, due to the axial stress along the drawing direction (**Figure 2e**, **2f**, and Table S8). Moreover, as shown in Figure S26, the XRD patterns perpendicular to the drawing direction show the obvious 002 peaks, while the 002 peaks are disappeared according to the XRD patterns parallel to the drawing direction, further confirming the MXene fibers with high orientation order along the axis of fibers. Simultaneously, because of the increase of the perpendicular stress, the porosity of the macroscopic CCM fibers is sharply reduced from 10.3% to 4.9% (**Figure 2g** and Figure S27). Similarly, CNM fibers also exhibit a high *f* of 0.83 and a low porosity of 7.4% for CNM-IV fiber, due to the stresses of thermal drawing (Figure S25, S28-30, and Table S9).

2.4. Interpretation of mechanical behavior in the thermal drawing process

Finite element analysis was performed to study the impact of drawing-induced stresses in the fabrication of MXene fibers with a COC protective layer using the Abaqus software. A CCM fiber model, including a COC hollow tube and an inner CMXene fiber over a total length of 1 mm, was established to understand the mechanical behavior of MXene fibers during the thermal drawing process (Figure S31). According to the experiments, lots of voids were generated by the removal of PC solvent as well as the partial hydroxyl surface terminations

and intercalated water at the temperature of ~220 ºC. Here, the porosity of about 16% was introduced into the inner CMXene fiber in the CCM fiber model. Upon application of the drawing force to the bottom of the COC hollow tube, the COC/CMXene model underwent stretching, resulting in a decrease in the diameter of the COC tube (Movie S2). The axial and perpendicular stress applied on the inner MXene fiber were generated due to the stresses from the COC protective layer (**Figure 3a**). Consequently, the axial stress induced by the thermal drawing process promoted the orientation of inner CMXene fibers, while the perpendicular stress from the COC protective layer led to a reduction in its porosity. Moreover, when increasing the draw-down ratio shown in **Figure 3b**, the axial stress applied on inner CMXene fibers was significantly increased to further promote the alignment of MXene nanosheets according to the simulation results. Meanwhile, by increasing the draw-down ratio, the introduced voids in inner MXene fiber were reduced by the increasing perpendicular stress, resulting in low porosity, consistent with the experimental porosity shown in Figure S32. Such combined effects lead to the enhanced compact microstructures of CCM fibers with high mechanical and electrical properties. As shown in Figure S33-36, both cross-sections of CCM-IV and CNM-IV fibers with few voids show smooth ultra-compact microstructures with increased draw-down ratios. Moreover, the existence of Ti, O, C, F, and N elements for the inner fibers proves the successful fabrication of CCM and CNM fibers from NMXene and CMXene nanosheets. And the obtained morphologies of MXene fibers confirm the results of the high orientation and low porosity evaluated from the WAXS/SAXS patterns.

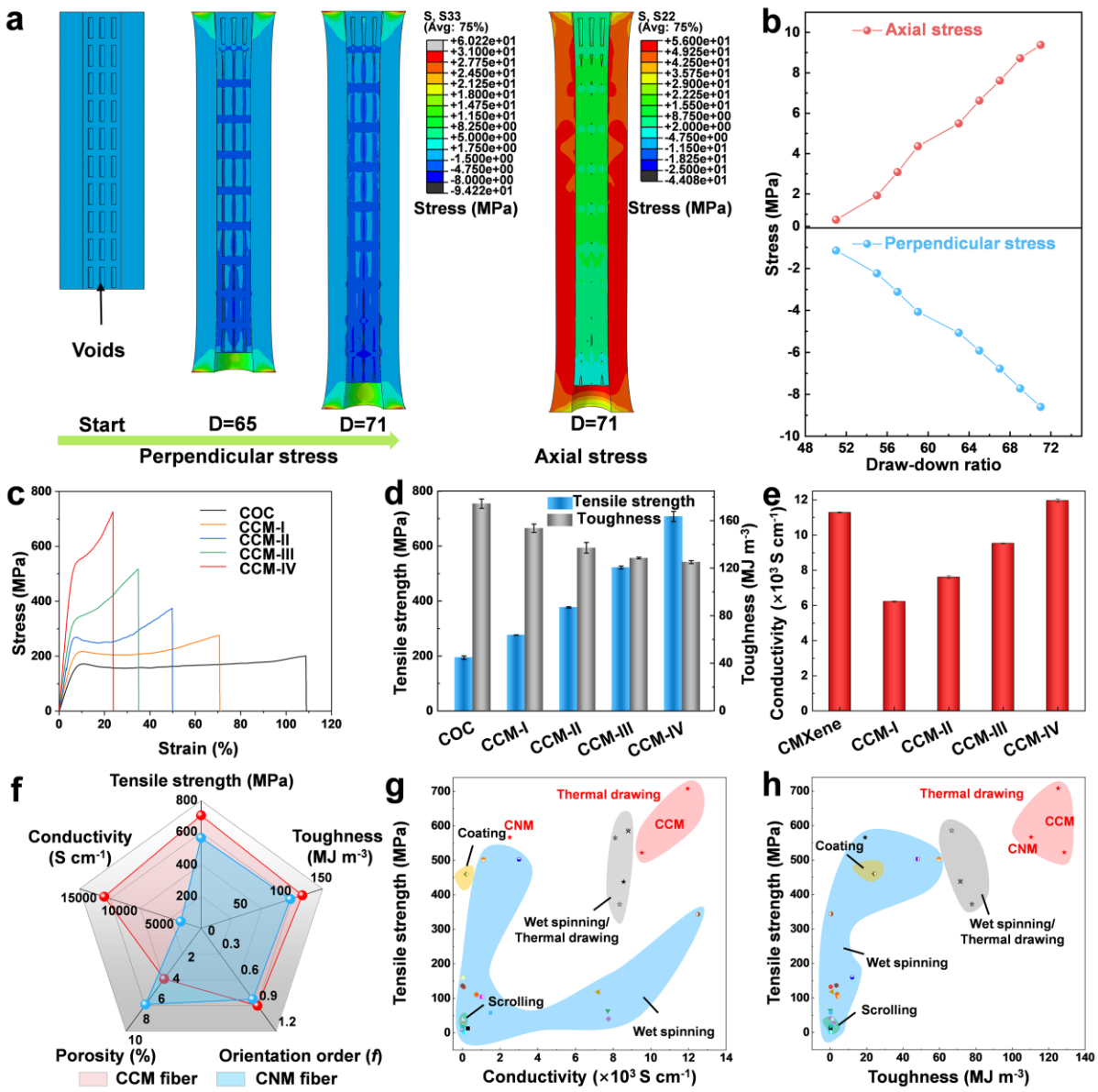

Figure 3. Mechanical and electrical properties of MXene fibers. a, Stress distribution of the simulation of finite element analysis. **b**, Axial and perpendicular stresses as the draw-down ratios increase during thermal drawing according to finite element analysis. **c**, Stress-strain curves of CCM fibers at various draw-down ratios. **d**, Tensile strength and toughness of CCM fibers. **e**, Electrical conductivity of CCM fibers. **f**, Star-plot of the performance for CCM and CNM fibers, including tensile strength, toughness, conductivity, orientation order, and porosity. Comparison of tensile strength vs. conductivity (**g**) and tensile strength vs. toughness (**h**) of the prepared strong macroscopic MXene fibers with reported MXene-based fibers through various prepared strategies.

2.5. Mechanical and electrical properties of MXene fibers

Because of the enhanced orientations of inner MXene fibers and COC chains, as well as the formation of tablet interlocks between the COC layer and MXene nanosheets, the strong CCM fibers prepared through various draw-down ratios exhibit high tensile strength from 276.08 ± 0.45 MPa for CCM-I fiber to 707.73 ± 18.33 MPa for CCM-IV fiber (Movie S3 and **Figure 3c**), including high toughness from 153.63 ± 3.50 MJ m^{-3} to 125.12 ± 1.29 MJ m^{-3} (**Figure 3d** and Figure S37). Moreover, the CCM-IV fiber offers the highest tensile strength, five times higher than that of the pure CMXene fibers fabricated by wet spinning with 140.39 ± 3.17 MPa, as well as a toughness 240 times stronger than that of pure MXene fibers of 0.52 ± 0.04 MJ m^{-3} (Table S10). Moreover, the electrical conductivity of the inner MXene fibers for CCM fibers increases from 6,216.2 ± 42.3 S cm^{-1} to 11,959.4 ± 97.4 S cm^{-1} with the draw-down ratio from 65 to 71, as shown in **Figure 3e** and Table S11. The CCM-IV fiber shows improved electrical conductivity compared to that of the pure MXene fibers with 11,282.2 ± 34.4 S cm^{-1} through wet spinning. This is due to the enhanced orientation and the reduction of porosity for inner MXene fibers with the in-situ removal of the partial hydroxyl surface terminations and intercalated water of CMXene nanosheets, as well as no crosslinkers through the thermal drawing. Similarly, for CNM fibers, CNM-IV fiber achieves a high tensile strength of 566.55 ± 1.21 MPa and toughness of 110.32 ± 2.99 MJ m^{-3}, higher than that of pure NMXene fiber through wet spinning with 102.06 ± 4.67 MPa and 0.50 ± 0.03 MJ m^{-3} (Figure S38, S39, and Table S12). In addition, the inner NMXene fibers for CNM fibers offer a high electrical conductivity of up to 2,512.5 ± 53.9 S cm^{-1}, which is again attributed to the significant decrease in voids and improvement of the orientation (Figure S40 and Table S13).

Additionally, as shown in Figure S41 and S42, the cyclic loading behavior of CCM and CNM fibers were also studied under different loading stress. For example, after subjecting CCM fibers to loading stress of 200 MPa for 3,000 cycles, the retention rate of electrical conductivity for the CCM-IV fiber remains high at 96.8%, and even 85.6% when the loading stress is increased to 400 MPa after 3,000 cycles (Table S14). Furthermore, when loading 550 MPa after 3,000 cycles, the CCM-IV fiber keeps a retention rate of 70.2%. Meanwhile, for CNM-IV fiber after 150 MPa loading stress, the retention rate remains high at 93.4%, and even 65.8% when the loading stress is increased to 480 MPa after 3,000 cycles (Table S15). These results are attributed to the compact tablet-interlocking microstructures for CCM and CNM fibers with low porosity and high orientation by thermal drawing-induced stresses. Therefore, the obtained CMM and CNM fibers show an overall improved performance,

including tensile strength, toughness, electrical conductivity, orientation, and porosity, as shown in **Figure 3f**. More importantly, in comparison to those of reported MXene fibers using different fabrication strategies, the resulting macroscopic fibers directly prepared by thermal drawing exhibit the highest properties in both tensile strength and conductivity,[5-8,11-15,17,22-24,36-42] as summarized in **Figure 3g** and Table S16. In particular, the macroscopic fibers with a COC protective layer offer ultra-high tensile strength and toughness of ~125.12 MJ m^{-3}, higher than those of reported MXene-based fibers with or without a protective layer (**Figure 3h**), CNT fibers, and graphene-based fibers (Table S17).

2.6. Fracture mechanism of COC-MXene fibers

Because of the collective effects of the axial and perpendicular stress induced by thermal drawing, the compact microstructures of CCM and CNM fibers by generating tablet interlocks in-situ are achieved with high orientation and low porosity to significantly improve their mechanical and electrical properties according to the cross-section of CCM fiber, as the FIB-SEM images shown in **Figure 4a**, **4b**, and Figure S43. Clearly, tablet interlocks are generated at the interface layer between the outer protective COC layer and inner MXene fibers. Moreover, over the fiber length, all the tablet interlocks are formed parallel to the fiber axis with the length size of 56.6 ± 16.2 μm and wide size of 7.3 ± 1.3 μm (Figure S44). According to the top SEM image, there are about eight tablet interlocks formed parallel to the fiber axis for the whole CCM fibers per 250 μm. With the assistance of such tablet-interlocking, the fracture mechanism of CCM fibers with a COC protective layer is illustrated in **Figure 4c**. When stretching starts, the wrinkled COC polymer chains of the protective layer and the inner MXene nanosheets are first straightened, which further enhances the orientation and reduces the voids of CCM fibers. In this step, there is no typical brittle fracture behavior of the inner MXene fibers, according to the smooth stress-strain curves (Figure 3c). This is attributed to the high orientation and low porosity of fibers as well as the tablet interlocking at the interface layer and hydrogen bonds between MXene nanosheets. Then, with further increased loading stress, the COC polymer chains are continuously stretched to protect the inner MXene fibers, followed by the sliding between MXene nanosheets of the inner MXene fibers along with the breakage of hydrogen bonds.[43] However, the tablet interlocking at the interface layer resists the formation of fracture, similar to the natural nacre.[44] Finally, under further stretching, inner MXene nanosheets start to separate from each other, and the COC polymer chains are eventually broken. As illustrated in **Figure 4d** and Figure S45, the tablet interlocks retained at the interface layer, and no

separation occurred between COC and MXene nanosheets after the fracture. Away from the tablet interlocks, MXene nanosheets underwent significant sliding, while lots of cracks appeared on the outer protective COC layer, confirming the fracture mechanism. The synergetic effects of the promoted alignment of COC chains, sliding impact on the compact MXene nanosheets, and tablet interlocking at the interface layer could accelerate the load transfer and dissipate stress energy for the CCM fiber to against the fracture.

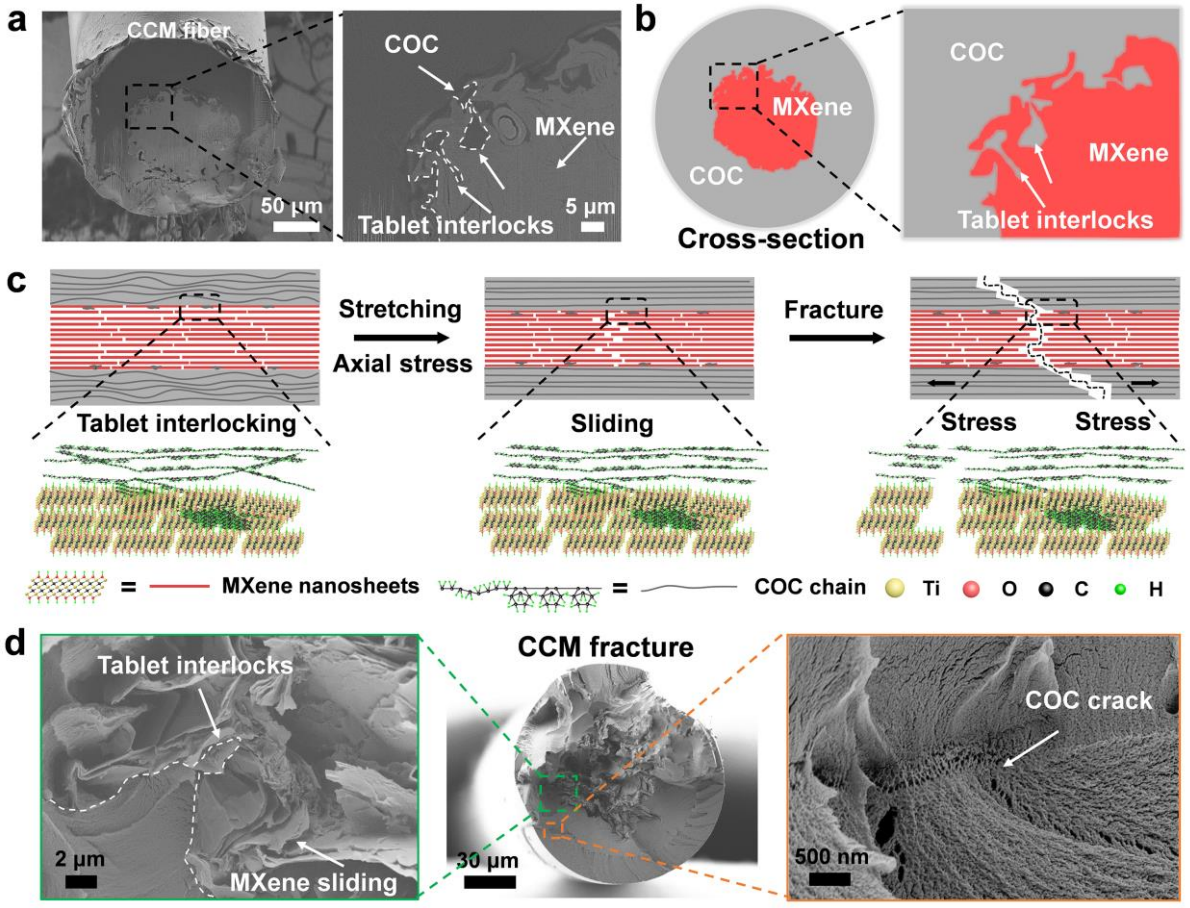

Figure 4. Fracture mechanism of COC-MXene fibers. a, Cross-section image of CCM fibers obtained via FIB-SEM. **b**, An illustration of the cross-section of CCM fiber with tablet interlocks between the COC layer and MXene nanosheets. **c**, Fracture mechanism of the CCM fibers due to the tablet interlocking at the interface layer, the sliding between MXene nanosheets, and the crack of the protective COC layer. **d**, Fracture morphology of the cross-section of CCM fibers, including the retention of tablet interlocks, sliding between MXene nanosheets, and COC crack.

2.7. Large-scale woven textiles for electromagnetic interference shielding

Owing to the booming development of the widespread use of telecommunication and portable electronic devices, the directly caused electromagnetic concerns should be considered

because of the harmful impact on human beings' health, as well as data misinterpretation, data loss, and even system failure, particularly when these devices are in close proximity to each other and suffer from strong electromagnetic induction effects.[34,45] Benefiting from the outstanding performance of MXene nanosheets, in addition to their high tensile strength, toughness, and electrical conductivity, both the CCM and CNM fibers possess promising potential as effective electromagnetic interference (EMI) shielding materials due to their high shielding efficiency (SE). Based on the high flexibility of the obtained strong fibers (Table S18), meter-scale textiles (3.0 m by 0.4 m) were successfully plain-woven by machine loom with cotton yarn as the warp and the MXene fibers as the weft (**Figure 5a** and Figure S46).

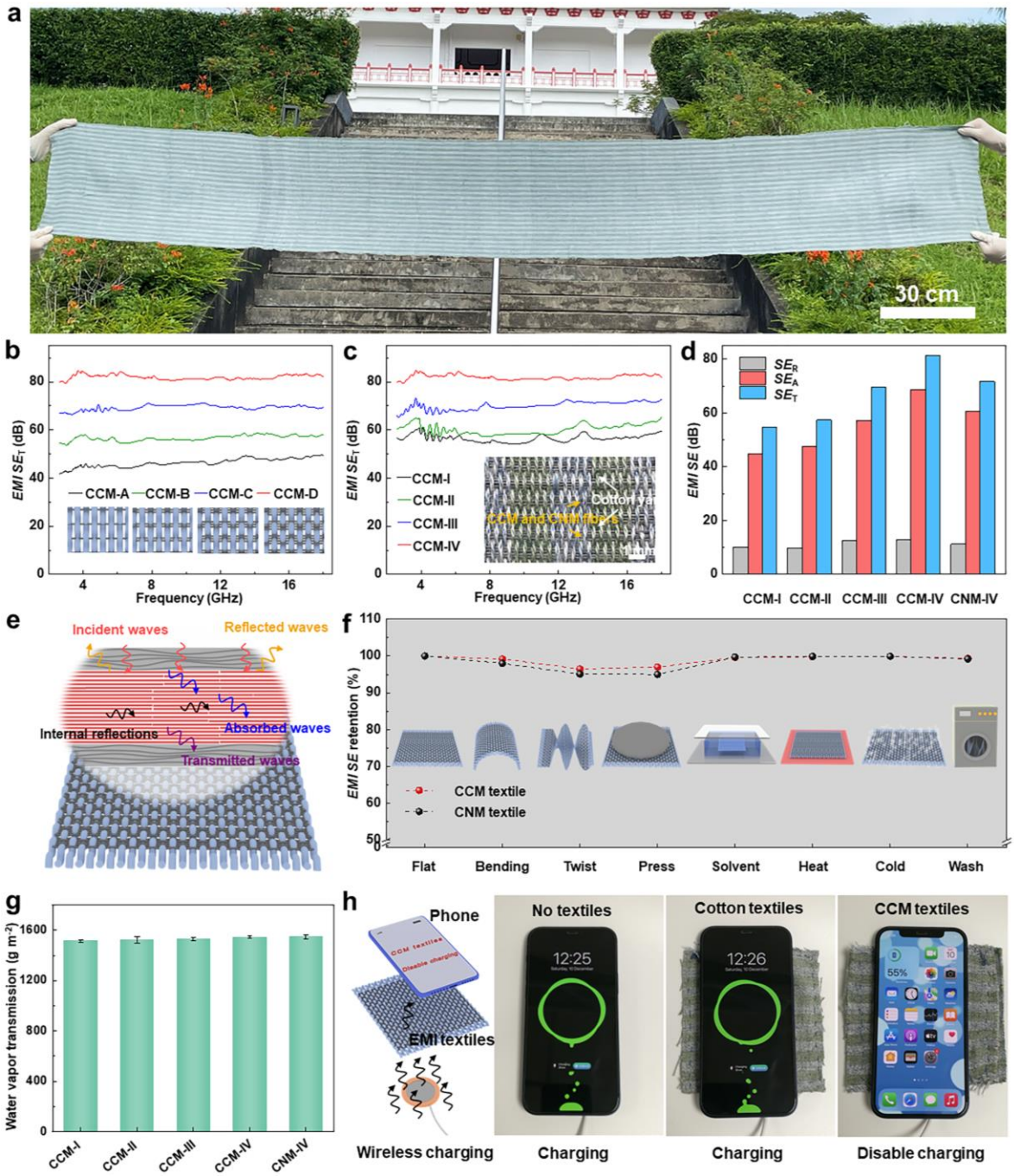

Figure 5. Large-scale woven textiles for EMI shielding. **a**, Large-scale textile woven by CCM fibers and cotton yarn with the size of 0.4 m by 3.0 m. **b**, *EMI SE*$_T$ of the textiles with different weft densities of CCM-IV fibers at the frequency of 2.6 GHz to 18.0 GHz. **c**, *EMI SE*$_T$ of the textiles based on CCM fiber at different draw-down ratios. **d**, *EMI SE* of the textiles based on CCM and CNM fibers at the frequency of 8.0 GHz. **e**, EMI shielding mechanism for the textiles prepared by CCM and CNM fibers. **f**, Durability and stability for the obtained textiles under different extreme environments. **g**, Water vapor transmission of woven textiles. **h**, Demonstration of the EMI shielding textiles for disabling the wireless charging of the phone.

As shown in **Figure 5b**, the EMI SE performance of woven textiles with various weft densities of CCM-IV fibers in the range of 76 to 229 fibers per inch (need to define CCM-A to CCM-D) was measured at the frequency of 2.6 GHz to 18.0 GHz (Figure S47). The EMI SE performance, including total *EMI SE* (SE_T), absorption *EMI SE* (SE_A), and reflection *EMI SE* (SE_R), of the obtained textiles is shown in Figure S48. Particularly, CCM-D has an EMI SE_T of ~81.5 dB, higher than other textiles of ~46.2 dB, ~56.5 dB, and ~70.5 dB at the frequency of 8.0 GHz because of the increase of the weft density for the CCM fibers. Also, the SE_A of all the textile samples (~36.5 dB, ~45.5 dB, ~59.0 dB, and ~68.8 dB) are higher than the SE_R (~9.7 dB, ~11.1 dB, ~11.6 dB, and ~12.8 dB) at the frequency of 8.0 GHz, respectively. These results indicate that the that the primary EMI shielding mechanism inside the MXene nanosheets of fibers is significantly based on the absorption of electromagnetic waves (EMWs). Furthermore, for the optimized weft density of CCM-D with 229 fibers per inch, the EMI SE property of textiles is evaluated with the fibers from CCM-I to CCM-IV prepared at various draw-down ratios, as shown in **Figure 5c** and **5d**. The CCM-IV textile shows a SE_T of ~81.5 dB, higher than that of CCM-I, CCM-II, and CCM-III textiles with ~54.7 dB, ~57.4 dB, and ~69.7 dB at 8.0 GHz, owing to its high electrical conductivity resulting from the high orientation and low porosity. Also, the SE_A of all textiles samples is higher than the SE_R, confirming the absorption mechanism inside the MXene nanosheets of fibers for the EMI shielding (Figure S48).

Apart from the CCM textiles, the woven textiles from CNM fibers also present a high EMI SE_T from ~47.63 dB to ~71.7 dB at 8.0 GHz with the increasing draw-down ratio from 65 to 71, accompanied by that SE_A is higher than SE_R with high intrinsic absorption capabilities (Figure S49). However, as shown Figure S50, it is evident that the reflection (*R*) of the plain-woven textiles prepared with various weft densities of CCM fibers, ranging from 76 to 229 fibers per inch, is higher than absorption (*A)* and transmission (*T*) at the frequency of 2.6 GHz-18.0 GHz and 8.0 GHz. Additionally, for woven CCM-I textiles to woven CCM-IV textiles, *R* increases from 0.90 to 0.95, while *A* decreases from 0.10 to 0.05, and *T* decrease to ~0 at the frequency of 8.0 GHz. Despite their high absorption inside the MXene nanosheets of fibers, all woven textiles based on CCM and CNM fibers (Figure S51) show *R* much higher than *A*, suggesting that the overall shielding performance mainly originates from reflection rather than absorption.[46,47] The reason for this might be attributed to the impedance mismatch between the MXene fibers and free space, leading to the reflection of

most incoming microwaves before their absorption.[47] Therefore, the overall EMI shielding mechanism of CCM and CNM textiles can be described in **Figure 5e** as follows:[4] To begin, the incident EMWs strike the surface of a MXene fiber in the textiles, some of them are immediately reflected due to the impedance mismatch between the highly conductive MXene nanosheets with the abundant free electrons and air.[47] Next, the residual waves can penetrate the lattice structure of MXene nanosheets in the fibers, interact with the high electron density of MXene nanosheets, and generate currents that dissipate the energy of the EMWs through the ohmic losses. When the EMWs pass through the initial layer of MXene nanosheets, the remaining EMWs continue to encounter the subsequent MXene barrier layer, resulting in a repeated attenuation of the EMWs. At the same time, the surviving EMWs are reflected by the second layer surface, causing multiple internal reflections. At last, the EMWs undergo back-and-forth reflections before being fully absorbed within the compact layers of MXene fibers. As a result, compared to other reported MXene-based materials in the literature, the obtained textiles from CCM and CNM fibers not only show high tensile strength and toughness, but also exhibit high specific shielding effectiveness per thickness (SSE_t)[4] of 5.2×10^4 dB cm^2g^{-1} for CMM textile and 4.7×10^4 dB cm^2g^{-1} for CNM textile, as summarized in Table S19.

Next, to meet the requirements for the actual application of textiles with MXene fibers, a test of the durability and stability of the woven textiles was conducted to evaluate their practicability. Due to the compact microstructures of CCM and CNM fibers with high orientation and low porosity, the woven textiles indeed exhibited excellent bending durability and stability, as shown in Figure S52. Whenever the textiles were encountered bending at the vertical middle, horizontal middle, and diagonal lines, the woven textiles from CCM and CNM fibers achieved the *EMI SE* retention over 99.0% and 96.8% at 8.0 GHz after 20,000 cycles of folding. Moreover, the woven textiles deformed into a twisted shape still performed an *EMI SE* retention of over 95% at 8.0 GHz after 10,000 cycles of bending for CCM and CNM fibers. When subjected to a 1.5 kg loading press with 0 to 2 folds for 24 h (Figure S53), the *EMI SE* of textiles from CCM and CNM fibers kept the retention of ~97.0% and ~95.0%, respectively. The excellent mechanical durability and stability are attributed to the interlocking-enabled compact microstructures of CCM/CNM fibers with high tensile strength and toughness.

Furthermore, the *EMI SE* retention of ~100% at 8.0 GHz remained for the woven textiles

from CCM and CNM fibers when stored in cold and hot environments at temperatures from -196 ºC to 160 ºC for 24 hours. After the woven textiles were stored at -100 ºC and 160 ºC for 32 days, the EMI SE of the woven textiles also remained without obvious variability (Figure S54). The remarkable stability in cold and hot environments is due to the contribution of the outside COC protective layer and inner compact MXene fibers. Additionally, because of the good corrosion resistance of the COC polymer in most solvents, the woven textiles from CCM and CNM fibers exhibited the outstanding resistance for most solvents and even for pH=13 and pH=-1 (Figure S55). After being immersed in various solvents for 24 hours, the textiles maintained an *EMI SE* retention of ~100%, indicating their practicability in different solvent environments. Moreover, to meet the application for use by human beings in our daily lives, the washing durability of the woven textiles was also tested by using a home washing machine according to the ISO 6330 standard, as presented in Figure S56. After 80 cycles of washing, the obtained textiles offered stable EMI SE retention to be compatible with human beings' daily applications. Therefore, the woven textiles from CCM and CNM fibers showed remarkable durability and stability with high *EMI SE* retention under various extreme environments (**Figure 5f**). Moreover, two types of woven textiles from CCM and CNM fibers were measured for moisture vapor transmission rate (MVTR) and drape behavior. As a result, the textiles from CCM-IV and CCN-IV fibers showed the drape coefficient of 45.8 ± 2.5% and 43.5 ± 3.2% (Figure S57), and the water vapor transmission of 1544.9 ± 12.52 g m^{-2} and 1546.32 ± 14.56 g m^{-2} (**Figure 5g**). Eventually, with their high tensile strength, toughness, and EMI properties, the woven EMI textiles from CCM fibers acted as a shielding barrier to effectively disable the wireless charging for the phone (**Figure 5h** and Movie S4) and even shield after serious deformation (Movie S5). Consequently, by leveraging their outstanding mechanical and electrical properties, the woven textiles prepared from strong MXene fibers with a COC protective layer could potentially be applied for personal protection for EMI shielding in people's daily lives and aerospace.

3. Conclusion

This work demonstrated a continuous strategy to directly prepare strong macroscopic MXene fibers with the in-situ generated COC protective layer and tablet interlocks at the interface layer by fluidics-assisted thermal drawing. Thanks to the axial and perpendicular stresses induced by thermal drawing, the alignments of COC polymer chains and inner MXene fibers were significantly promoted together with largely reduced porosity between MXene nanosheets. As a result, the resulting macroscopic MXene fibers with compact microstructure

not only performed with ultra-high tensile strength and toughness, but also showed outstanding electrical conductivity for the inner MXene fiber. The fracture mechanism was studied, owing to the tablet interlocking at the interface layer, sliding impact on the compact MXene nanosheets with high orientation and low porosity, and the crack of the promoted alignment of COC chains. Then, the woven textiles from two kinds of MXene fibers with remarkable EMI shielding performance worked effectively to enable large-scale applications, even in various extreme environments with superior durability and stability. The results reveal that the demonstrated strategy provides a universal route to manufacture strong fibers with compact microstructure and excellent properties, paving the way toward smart textiles. Indeed, a great number of multifunctional fibers can be generally prepared through such an effective strategy from various nanostructured functional materials, ultimately enhancing their performance and applicability to meet diverse requirements.

4. Methods

Materials. Raw MAX materials, including Ti_3AlC_2 and Ti_3AlCN powders (particle size ~ 400 mesh), were purchased from Jilin 11 Technology Co. Ltd. Lithium fluoride and propylene carbonate (PC) were obtained from Sigma-Aldrich Co., Ltd. Cyclic olefin copolymer (COC, 6013M-07) was purchased from Polyplastics CO., Ltd. All materials were used as received.

Characterization. SEM images were obtained using a Schottky field emission scanning electron microscopes (JEOL JSM-7600F) with a voltage of 5 kV. High-resolution transmission electron microscope (HR-TEM) images were obtained via a Grand ARM instrument (ACTEM JEOL JEM-ARM300F) using an acceleration voltage of 300 kV. A Park NX10 atomic force microscope was used to obtain AFM images. TGA results were performed under nitrogen using thermogravimetric analyzer (Q500 SDT) at a heating rate of 10 ºC min^{-1} from 35 ℃ to 800 ℃. X-ray diffraction (XRD) patterns were obtained with Cu-Kα radiation using an XRD Bruker D8 Advance. The rheological properties of the MXene/PC slurry were acquired with a rheometer (TA HR10) using steady shear and dynamic oscillatory conditions with in-situ heating from 25 ℃ to 220 ℃, and from 160 ℃ to 260 ℃ for COC polymer. The viscoelastic properties of the slurry were tested by performing the storage and loss modulus evaluation as a function of frequency from 0.1 to 100 rad s^{-1}. In addition, the strain amplitude was kept at 0.1% with a gap of 1 mm for the frequency sweep.

Polarized optical microscopy (POM) images were obtained to show optical birefringence using optical microscope (Olympus BX51). FTIR spectra were obtained at room temperature with Diamond ATR via an FTIR Frontier (PerkinElmer). XPS spectra were acquired by using an XPS Kratos AXIS Supra. Electrical conductivities were measured via a standard two-probe method using a Keithley 2700 source meter. WAXS/SAXS patterns were acquired on a SWAXS Xenocs Nano-inXider utilizing a Cu-Kα source (conducted at 30 W) with a beam diameter from 200 to 800 mm on SAXS (200 K) and WAXS (100 K) detectors. Three samples were tested for each CCM and CNM fibers to evaluate the orientation order (*f*) of fibers. In-situ XRD patterns at different temperatures were performed by the Linkam temperature stage using a SWAXS Xenocs Nano-inXider. In order to calculate the porosity of each CCM and CNM fibers, three samples of each CCM and CNM fibers were tested to obtain the XRD patterns using a SWAXS Xenocs Nano-inXider. The fibers were placed horizontally and perpendicularly beneath the X-ray to test XRD patterns. The cross-sectional

morphology of CCM and CNM fibers was conducted using ZEISS Crossbeam 540 FIB-SEM microscope with focused ion beam (FIB). Tensile stress-strain curves were tested on 20 mm × 3 mm (long × wide) samples via a SUNS EUT4103X Tester with a 100 N sensor using loading rate of 0.3 mm min^{-1} at room temperature. At the same time, the mechanical properties of pure MXene fibers obtained by wet spinning were conducted with a 10 N sensor. The cross-sectional area of fibers was obtained by FIB-SEM. The results for each fiber were calculated using the average value of three samples.

Preparation of COC-MXene fibers via thermal drawing. The cyclic olefin copolymer (COC) hollow tube was sealed by a thin polytetrafluoroethylene (PTFE) filtration film with a pore diameter of 0.45 μm, and baked in the vacuum oven at 100 °C for one week to remove the residual water. Before thermal drawing, the MXene/PC slurry with concentrations of 120-160 mg mL^{-1} was injected into the COC hollow tube. Then, the prepared rod of COC tube with a slurry was inserted into a two-zone heating furnace with the top/bottom zones heated at 170 °C/360 °C. Finally, the MXene fibers with COC protective layer were prepared with various draw-down ratios (*D*) from 65-71. The *D* is calculated as follows:

$$D=\sqrt{\frac{v_D}{v_F}} \tag{1}$$

where v_D and v_F are the drawing and feeding speeds, respectively.

Finite element analysis of MXene/COC fibers via the thermal drawing. The MXene/COC fibers model was constructed via the commercial software Abaqus/CAE 2019 with Abaqus/Explicit. The mechanical behavior of the inner-MXene fibers were analyzed after the volatilization of PC solvent from the hot zone at the temperature of ~220 ºC. Many voids were generated when the MXene/COC fibers passed through the hot zone. Moreover, pure CMXene fibers have the porosity of 15.3% at 220 ºC based on the in-situ XRD results. Therefore, after the volatilization of PC solvent at the hot zone with the temperature of ~220 ºC, the MXene/COC fibers model was created with about 16% of porosity for the inner MXene fibers in this simulation. Moreover, a diameter of 0.31 mm for the COC hollow tube with an inner diameter of 0.15 mm for inner MXene fiber and a total length of 1.0 mm was constructed to perform the mechanical testing of MXene fibers during thermal drawing. A SUNS EUT4103X Tester characterized the mechanical properties of COC hollow tubes with a 100 N sensor at the temperature of 220 °C.

The mechanical tests of the COC hollow tubes show that the tubes have an isotropic bulk modulus (E_{COC}) of 0.30 GPa and Poisson's ratio (υ_{COC}) of 0.35. In addition, the inner MXene

fibers have the isotropic bulk modulus (E_M) of 0.5 GPa and the Poisson's ratio (υ_M) of 0.3 with the porosity of 16%. During the simulation, the fixed boundary conditions were set at the top of the MXene/COC hollow tube, while the pulling force was applied at the bottom of the COC hollow tube. Furthermore, the applied pulling force was the same as the conditions of the experiments to study the mechanical behavior of an increasing draw-down ratios via thermal drawing. The inner MXene fibers and COC tube model could be defined according to equation 2 and 3 with isotropic elasticity-plasticity of as follows:

$$\begin{Bmatrix} \varepsilon_{11} \\ \varepsilon_{22} \\ \varepsilon_{33} \\ \gamma_{12} \\ \gamma_{13} \\ \gamma_{23} \end{Bmatrix} = \begin{bmatrix} 1/E_m & -\upsilon/E_m & -\upsilon/E_m & 0 & 0 & 0 \\ -\upsilon/E_m & 1/E_m & -\upsilon/E_m & 0 & 0 & 0 \\ -\upsilon/E_m & -\upsilon/E_m & 1/E_m & 0 & 0 & 0 \\ 0 & 0 & 0 & 1/G_m & 0 & 0 \\ 0 & 0 & 0 & 0 & 1/G_m & 0 \\ 0 & 0 & 0 & 0 & 0 & 1/G_m \end{bmatrix} \begin{Bmatrix} \sigma_{11} \\ \sigma_{22} \\ \sigma_{33} \\ \sigma_{12} \\ \sigma_{13} \\ \sigma_{23} \end{Bmatrix} \quad (2)$$

$$G_m = \frac{E_m}{2\times(1+\lambda)} \quad (3)$$

where G_m, E_m, and λ are the shear modulus, Young's modulus, and Poisson's ratio of the materials such as MXene fiber and COC tubes, respectively.

Fabrication of the textiles. The plain-woven textiles were obtained by using a semi-automatic loom of Y208W (Nantong Sansi Technology Co., LTD) constructed with the cotton yarns as warp and the CCM and CNM fibers as weft. To prepare the textiles with different weft densities of MXene fibers, the warp density was kept 60 yarns per inch. Subsequently, the textiles were weaved with the weft density of 76-229 MXene fibers per inch, denoted as 76 fibers for CCM-A, 127 fibers for CCM-B, 178 fibers for CCM-C, and 229 fibers for CCM-D, respectively.

Measurement for electromagnetic interference (EMI) shielding performance. The woven textiles, composed of CCM and CNM fibers, were prepared for EMI shielding test with a DR-WX rectangular waveguide using the N9917A network analyzer (Agilent Technologies, USA) at the frequency range of 2.6 GHz to 18.0 GHz. The strong CCM and CNM fibers were weaved into the rectangular shape textiles for the test.

The ability to attenuate the energy of the incident electromagnetic waves for the prepared textiles based on CCM and CNM fibers is calculated as *EMI SE*. It is important for the electromagnetic interference shielding device to block electromagnetic radiation that could be harmful to electronic devices. The absorption (*A*), reflection (*R*), and transmission (*T*) should add up to 1 when the electromagnetic radiation interacts with a shielding material, presenting

the shielding phenomenon as:

$$A+R+T=1 \quad (4)$$

Furthermore, the scattering parameters (S_{22}, S_{11}, S_{21}, and S_{12}) were directly obtained from the network analyzer to calculate the corresponding reflection (R) and transmission (T) coefficients using the equation 5 and 6:

$$R=|S_{22}|^2=|S_{11}|^2 \quad (5)$$

$$T=|S_{21}|^2=|S_{12}|^2 \quad (6)$$

Consequently, the expressions for the shielding reflection (SE_R) and absorption (SE_A) can be formulated by considering the reflection and effective absorption of incident electromagnetic waves inside the shielding material according to the coefficients of R and T as follows:

$$SE_R=10\log\left(\frac{1}{1-R}\right)=10\log\left(\frac{1}{1-|S_{11}|^2}\right) \quad (7)$$

$$SE_A=10\log\left(\frac{1-R}{T}\right)=10\log\left(\frac{1-|S_{11}|^2}{|S_{21}|^2}\right) \quad (8)$$

Additionally, when EMI SE is more than 15 dB, the multiple internal reflections are generally negligible. Therefore, the total EMI SE_T is the sum of reflection (SE_R) and absorption (SE_A), estimated as follows:

$$SE_T=SE_R+SE_A \quad (9)$$

Moreover, the specific shielding effectiveness per thickness (SSE_t) of the woven textiles could be evaluated using the equation 10:

$$SSE_t=\frac{SE_T}{\rho_t t} \quad (10)$$

where ρ_t is the density and of the woven textiles, and t is the thickness of the inner MXene fibers of CCM and CNM fibers.

Testing the performance of the woven textiles. The washing procedure for textiles was performed according to the standard of ISO 6330 via domestic washing and drying. The home washing machine of MT740S (Midea) with the anti-bacterial detergent (Yuri Distribution Co. Pte. Ltd) and the tested textiles were to set with the general program of a 2.3 kg load including a standard cycle of washing, rinsing, and spinning at the temperature of 40 ^oC for 50 minutes. After every 10 washing cycles, the electromagnetic interference (EMI) shielding efficiency (EMI SE) test of textiles was measured at the frequency from 2.6 GHz to 18.0 GHz, while the retention of EMI SE of washing was evaluated by analyzing data recorded at a frequency of 8.0 GHz. The moisture vapor transmission rate (MVTR) was conducted according to the ASTM E96 standard, using the samples of textiles with the same diameter of 68 mm mounted on top of the standardized cup containing 20 ml of distilled

water. The three identically sealed cups for each sample were prepared for the test in a relative humidity of 50% at 38 ºC for 24 h. Furthermore, the drape coefficient of the textiles was measured following the ISO 9073-9-2008 standard using image processing technology with the diameter of 30 cm for the textiles.

Acknowledgements

This work was supported by the Singapore Ministry of Education Academic Research Fund Tier 2 (MOE2019-T2-2-127 and MOE-T2EP50120-0002), the Singapore Ministry of Education Academic Research Fund Tier 1 (RG62/22), A*STAR under AME IRG (A2083c0062), and A*STAR under IAF-ICP Programme I2001E0067 and the Schaeffler Hub for Advanced Research at NTU. This work was supported by the IDMxS (Institute for Digital Molecular Analytics and Science) by the Singapore Ministry of Education under the Research Centres of Excellence scheme. This work was also supported by the NTU-PSL Joint Lab collaboration. This work was partly supported by the National Science Fund for Distinguished Young Scholars (52125302), the National Key Research and Development Program of China (2021YFA0715703), the National Natural Science Foundation of China (NSFC) (52203078, 22075009), the National Postdoctoral Program for Innovative Talents (BX2021025), and Postdoctoral Science Foundation (2021M690005). The authors acknowledge Professor Kye Yak See and Doctor Eng Kee Chua for providing the equipment for the test of EMI shielding.

Author contributions

T.Z.Z. and L.W. designed the research. T.Z.Z. conducted the fabrication and data analyses. T.Z.Z. and H.Z. carried out finite element analysis. C.C. assisted in the SEM test. J.Y. and Q.Z. assisted in the HR-TEM test. T.X., Z.W., and S.X.Y. assisted in the demonstration. T.Z.Z. and F.L. carried out the FTIR test. T.Z.Z., Q.F.C., and L.W. co-wrote the manuscript. And all the authors discussed the results and commented on the manuscript.

Received: ((will be filled in by the editorial staff))

Revised: ((will be filled in by the editorial staff))

Published online: ((will be filled in by the editorial staff))

References

[1] M. Naguib, M. Kurtoglu, V. Presser, J. Lu, J. Niu, M. Heon, L. Hultman, Y. Gogotsi, M. W. Barsoum, *Adv. Mater.* **2011**, *23*, 4248-4253.

[2] A. Lipatov, H. Lu, M. Alhabeb, B. Anasori, A. Gruverman, Y. Gogotsi, A. Sinitskii, *Sci. Adv.* **2018**, *4*, eaat0491.

[3] Y. Xia, T. S. Mathis, M. Zhao, B. Anasori, A. Dang, Z. Zhou, H. Cho, Y. Gogotsi, S. Yang, *Nature* **2018**, *557*, 409-412.

[4] F. Shahzad, M. Alhabeb, C. B. Hatter, B. Anasori, S. M. Hong, C. M. Koo, Y. Gogotsi, *Science* **2016**, *353*, 1137-1140.

[5] W. Eom, H. Shin, R. B. Ambade, S. H. Lee, K. H. Lee, D. J. Kang, T. H. Han, *Nat. Commun.* **2020**, *11*, 2825.

[6] H. Shin, W. Eom, K. H. Lee, W. Jeong, D. J. Kang, T. H. Han, *ACS Nano* **2021**, *15*, 3320-3329.

[7] J. Zhang, S. Uzun, S. Seyedin, P. A. Lynch, B. Akuzum, Z. Wang, S. Qin, M. Alhabeb, C. E. Shuck, W. Lei, E. C. Kumbur, W. Yang, X. Wang, G. Dion, J. M. Razal, Y. Gogotsi, *ACS Cent. Sci.* **2020**, *6*, 254-265.

[8] A. Levitt, J. Zhang, G. Dion, Y. Gogotsi, J. M. Razal, *Adv. Funct. Mater.* **2020**, *30*, 2000739.

[9] M. Hasan, M. S. B. Sadeque, I. Albasar, H. Pecenek, F. K. Dokan, M. S. Onses, M. Ordu, *Small* **2023**, *19*, 2206107.

[10] Q. Jiang, N. Kurra, M. Alhabeb, Y. Gogotsi, H. N. Alshareef, *Adv. Energy Mater.* **2018**, *8*, 1703043.

[11] Z. Wang, S. Qin, S. Seyedin, J. Zhang, J. Wang, A. Levitt, N. Li, C. Haines, R. Ovalle-Robles, W. Lei, Y. Gogotsi, R. H. Baughman, J. M. Razal, *Small* **2018**, *14*, 1802225.

[12] Q. Yang, Z. Xu, B. Fang, T. Huang, S. Cai, H. Chen, Y. Liu, K. Gopalsamy, W. Gao, C. Gao, *J. Mater. Chem. A* **2017**, *5*, 22113-22119.

[13] S. Seyedin, R. Yanza, J. Razal, *J. Mater. Chem. A* **2017**, *5*, 24076-24082.

[14] S. Li, Z. Fan, G. Wu, Y. Shao, Z. Xia, C. Wei, F. Shen, X. Tong, J. Yu, K. Chen, M. Wang, Y. Zhao, Z. Luo, M. Jian, J. Sun, R. B. Kaner, Y. Shao, *ACS Nano* **2021**, *15*, 7821-7832.

[15] W. Cao, C. Ma, D. Mao, J. Zhang, M. Ma, F. Chen, *Adv. Funct. Mater.* **2019**, *29*, 1905898.

[16] W. Shao, M. Tebyetekerwa, I. Marriam, W. Li, Y. Wu, S. Peng, S. Ramakrishna, S. Yang, M. Zhu, *J. Power Sources* **2018**, *396*, 683-690.

[17] B. Cheng, P. Wu, *ACS Nano* **2021**, *15*, 8676-8685.

[18] Z. Xu, Y. Liu, X. Zhao, L. Peng, H. Sun, Y. Xu, X. Ren, C. Jin, P. Xu, M. Wang, C. Gao, *Adv. Mater*. **2016**, *28*, 6449-6456.

[19] W. Weng, J. Yang, Y. Zhang, Y. Li, S. Yang, L. Zhu, M. Zhu, *Adv. Mater.* **2019**, *32*, 1902301.

[20] M. Chen, Z. Wang, Q. Zhang, Z. Wang, W. Liu, M. Chen, L. Wei, *Nat. Commun.* **2021**, *12*, 1416.

[21] C. Dong, A. Leber, T. D. Gupta, R. Chandran, M. Volpi, Y. Qu, T. Nguyen-Dang, N. Bartolomei, W. Yan, F. Sorin, *Nat. Commun.* **2020**, *11*, 3537.

[22] L. Wang, M. Zhang, B. Yang, J. Tan, *ACS Appl. Mater. Interfaces* **2021**, *13*, 41933-41945.

[23] L. Liu, W. Chen, H. Zhang, L. Ye, Z. Wang, Y. Zhang, P. Min, Z. Yu, *Nano-Micro Lett.* **2022**, *14*, 111.

[24] T. Zhou, Y. Yu, B. He, Z. Wang, T. Xiong, Z. Wang, Y. Liu, J. Xin, M. Qi, H. Zhang, X. Zhou, L. Gao, Q. Cheng, L. Wei, *Nat. Commun.* **2022**, *13*, 4564.

[25] Y. Ma, N. Liu, L. Li, X. Hu, Z. Zou, J. Wang, S. Luo, Y. Gao, *Nat. Commun.* **2017**, *8*, 1207.

[26] L. Ding, Y. Wei, L. Li, T. Zhang, H. Wang, J. Xue, L. Ding, S. Wang, J. Caro, Y. Gogotsi, *Nat. Commun.* **2018**, *9*, 155.

[27] Q. Zhang, H. Lai, R. Fan, P. Ji, X. Fu, H. Li, *ACS Nano* **2021**, *15*, 5249-5262.

[28] K. Maleski, V. Mochalin, Y. Gogotsi, *Chem. Matter.* **2017**, *29*, 1632-1640.

[29] B. Akuzum, K. Maleski, B. Anasori, P. Lelyukh, N. J. Alvarez, E. C. Kumbur, Y. Gogotsi, *ACS Nano* **2018**, *12*, 2685-2694.

[30] S. Naficy, R. Jalili, S. H. Aboutalebi, R. A. Gorkin III, K. Konstantinov, P. C. Innis, G. M. Spinks, P. Poulinc, G. G. Wallace, *Mater. Horiz.* **2014**, *1*, 326-331.

[31] B. Akuzum, K. Maleski, B. Anasori, P. Lelyukh, N. J. Alvarez, E. C. Kumbur, Y. Gogotsi, *ACS. Nano.* **2018**, *12*, 2685-2694.

[32] C. Zhu, X. Liu, X. Yu, N. Zhao, J. Liu, J. Xu, *Carbon* **2012**, 50, 235-243.

[33] A. F. Thünemann, W. Ruland, *Macromolecules* **2000**, 33, 1848-1852.

[34] A. Iqbal, F. Shahzad1, K. Hantanasirisakul, M. Kim, J. Kwon, J. Hong, H. Kim, D. Kim, Y. Gogotsi, C. M. Koo, *Science* **2020**, *369*, 446-450.

[35] G. Xin, W. Zhu, Y. Deng, J. Cheng, L. T. Zhang, A. J. Chung, S. De, J. Lian, *Nat. Nanotechnol.* **2019**, *14*, 168-175.

[36] Q. Liu, A. Zhao, X. He, Q. Li, J. Sun, Z. Lei, Z. Liu, *Adv. Funct. Mater.* **2021**, *31*,

2010944.

[37] J. Zhang, S. Seyedin, S. Qin, Z. Wang, S. Moradi, F. Yang, P. A. Lynch, W. Yang, J. Liu, X. Wang, J. M. Razal, *Small* **2019**, *15*, 1804732.

[38] N. He, S. Patil, J. Qu, J. Liao, F. Zhao, W. Gao, *ACS Appl. Energy Mater.* **2020**, *3*, 2949-2958.

[39] S. Seyedin, S. Uzun, A. Levitt, B. Anasori, G. Dion, Y. Gogotsi, J. M. Razal, *Adv. Funct. Mater.* **2020**, *30*, 1910504.

[40] Y. Li, X. Zhang, *Adv. Funct. Mater.* **2022**, *32*, 2107767.

[41] J. Gu, F. Li, Y. Zhu, D. Li, X. Liu, B. Wu, H. Wu, X. Fan, X. Ji, Y. Chen, J. Liang, *Adv. Mater.* **2023**, *35*, 2209527.

[42] C. Yu, Y. Gong, R. Chen, M. Zhang, J. Zhou, J. An, F. Lv, S. Guo, G. Sun, *Small* **2018**, *14*, 1801203.

[43] T. Zhou, C. Wu, Y. Wang, A. P. Tomsia, M. Li, E. Saiz, S. Fang, R. H. Baughman, L. Jiang, Q. Cheng, *Nat. Commun.* **2020**, *11*, 2077.

[44] U. Wegst, H. Bai, E. Saiz, A. P. Tomsia, R. O. Ritchie, *Nat. Mater.* **2015**, *14*, 23-36.

[45] W. Cao, F. Chen, Y. Zhu, Y. Zhang, Y. Jiang, M. Ma, F. Chen, *ACS Nano* **2018**, *12*, 4583-4593.

[46] M. H. Al-Saleh, H. Saadeh, U. Sundararaj, *Carbon* **2013**, *60*, 146-156.

[47] W. Yang, Z, Zhao, K. Wu, R. Huang, T. Liu, H. Jiang, F. Chen, Q. Fu, *J. Mater. Chem. C*, **2017**, *5*, 3748-3756.